Direct first-principles chemical potential calculations of liquids

Qi-Jun Hong and Axel van de Walle

Citation: J. Chem. Phys. **137**, 094114 (2012); doi: 10.1063/1.4749287
View online: http://dx.doi.org/10.1063/1.4749287
View Table of Contents: http://jcp.aip.org/resource/1/JCPSA6/v137/i9
Published by the American Institute of Physics.

Direct first-principles chemical potential calculations of liquids

Qi-Jun Hong[1,2,a)] and Axel van de Walle[2,3]
[1]*Division of Chemistry and Chemical Engineering, California Institute of Technology, Pasadena, California 91125, USA*
[2]*School of Engineering, Brown University, Providence, Rhode Island 02912, USA*
[3]*Department of Applied Physics and Materials Science, California Institute of Technology, Pasadena, California 91125, USA*

(Received 23 May 2012; accepted 17 August 2012; published online 7 September 2012)

We propose a scheme that drastically improves the efficiency of Widom's particle insertion method by efficiently sampling cavities while calculating the integrals providing the chemical potentials of a physical system. This idea enables us to calculate chemical potentials of liquids directly from first-principles without the help of any reference system, which is necessary in the commonly used thermodynamic integration method. As an example, we apply our scheme, combined with the density functional formalism, to the calculation of the chemical potential of liquid copper. The calculated chemical potential is further used to locate the melting temperature. The calculated results closely agree with experiments. © *2012 American Institute of Physics*. [http://dx.doi.org/10.1063/1.4749287]

I. INTRODUCTION

Free energy and chemical potential are of fundamental importance in thermodynamics, particularly in the study of phase equilibria. However, unlike quantities such as energy, temperature, and pressure, chemical potential is not in general possible to obtain directly by molecular dynamics (MD) or metropolis Monte Carlo (MC) simulations. Rather than simply computing the temporal average of an explicit function of dynamical variables, the value of chemical potential is related to an integral over the accessible phase space.[1,2] Although this problem can be fortunately circumvented for solid by an appropriate treatment of phonon density of states under the quasiharmonic approximation and further correction using the thermodynamic integration method, the complexity still persists for liquids due to the lack of a natural universal reference system.

Chemical potentials of liquids are usually calculated in an *indirect* approach, which connects the system of interest to a reference system with known chemical potential and then calculates the difference of the two systems by thermodynamic integration. The development of density functional theory (DFT)[3–5] has raised great interests to calculate chemical potentials and to study phase equilibia from first-principles. Car and Sugino,[6] pioneering in the field, successfully calculated the chemical potentials of liquid-state silicon and further computed the melting point within an error of 100 K. The method was then applied to liquid aluminum by de Wijs *et al.*[7] The melting point they calculated differs from the true value by less than 5%. Employing similar techniques, Alfè *et al.*[8,9] further simulated the melting of iron under Earth's core conditions. Since directly experimental measurement is challenging under such extreme conditions, their results can help determine the temperature of the Earth's inner core.

Despite of these successful examples, one apparent drawback of the thermodynamic integration method lies in its heavy dependence on the reference system, which is required to be sufficiently close to the actual system, so that the cost needed to compute the chemical potential difference would not be prohibitively expensive.[10] Unfortunately, such a reference system is not universally available. Even if it is obtainable, it would demand detailed study of material properties and precise fitting to *ab initio* results, which require a large amount of both computer and human effort. As a result, the application of this method is limited.

As an alternative approach, Widom's test-particle insertion scheme[11] is a popular method to *directly* calculate the chemical potential of a liquid. Chemical potential is calculated as an additional free energy, namely, a change of free energy after inserting one more particle. Consequently, the chemical potential is related to the ensemble average and integration of Boltzmann's factors $\exp(-\beta\Delta U)$, where ΔU is insertion energy, the energy change during particle insertion. In practice, the average is evaluated by occasionally inserting the test particle into the simulation volume, measuring ΔU and then removing it before continuing the simulation. This approach has been applied to some simple empirical potentials,[12–16] mostly Lennard-Jones potentials. The major problem of the Widom's method is that it is usually considered computationally too expensive, because most insertion attempts lead to a vanishingly small value of $\exp(-\beta\Delta U)$ (due to high energy cost of inserting the test-particle in a small cavity in the dense system) and the corresponding computational efforts are thus wasted. Probably because of the prohibitive computational cost, there have been apparently no attempts so far to compute first-principles chemical potential directly with Widom's method.

Nevertheless, compared to the thermodynamic integration approach, the Widom's method holds a great advantage, since it does not require any reference system. This property makes it possible to find a universal solution to first-principles

a)qhong@caltech.edu.

calculations of liquid-state chemical potentials. This is especially useful in automated materials screening effort in which melting point is a design parameter, since one does not need to develop empirical potentials for each of the chemical system explored. In this article, we revisit the Widom's particle insertion method and modify it with an efficient cavity-sampling scheme, which achieves a drastic reduction in computational cost. The theoretical backgrounds are described in Sec. II. Chemical potential and melting temperature calculations can be found in Sec. III. Discussions and future directions are presented in Sec. IV.

II. THEORY

A. Particle insertion method

We briefly reiterate the Widom's particle insertion method here. By definition, chemical potential μ is the partial derivative of free energy F with respect to number of particles N, $\mu_i = (\partial F/\partial N_i)_{V,T,N_{j\neq i}}$, where V is volume and T is temperature. Thus, it can be calculated by evaluating the additional free energy, namely the free energy change after inserting one more particle,

$$\mu_i = F(V, T, N_i + 1, N_{j\neq i}) - F(V, T, N_i, N_{j\neq i}) + O\left(\frac{\partial^2 F}{\partial N_i^2}\right). \quad (1)$$

The higher-order derivative, which leads to finite-size correction, will be discussed later in Sec. III A. Assume the system of interest contains N homogeneous atoms. The Helmholtz free energy of such a system is (using a classical partition function)

$$F(V, T, N) = -kT \ln\left(\frac{1}{\Lambda^{3N} N!}\int \exp\left[-\frac{U(\mathbf{r}^N)}{kT}\right] \mathrm{d}\mathbf{r}^N\right), \quad (2)$$

where k is the Boltzmann constant, Λ is de Broglie wavelength, $\Lambda = \sqrt{h^2/(2\pi mkT)}$, U is potential energy and r^N is a 3N-dimensional vector of atomic positions. Combining Eqs. (1) and (2), the expression for chemical potential can be written as

$$\mu \simeq \Delta F_{N\to N+1} = \mu_{\mathrm{id}} + \mu_{\mathrm{ex}}, \quad (3)$$

$$\mu_{\mathrm{id}} = -kT \ln\left(\frac{V}{\Lambda^3(N+1)}\right), \quad (4)$$

$$\mu_{\mathrm{ex}} = -kT \ln\left(\frac{1}{V}\frac{\int \exp[-U(\mathbf{r}^{N+1})/kT]\mathrm{d}\mathbf{r}^{N+1}}{\int \exp[-U(\mathbf{r}^N)/kT]\mathrm{d}\mathbf{r}^N}\right). \quad (5)$$

Notice that the approximation sign in Eq. (3) is due to the omission of higher-order derivative in Eq. (1), which we will discuss and correct later.

In Eq. (3), we separate the chemical potential into two parts, the ideal gas term μ_{id} and the excess term μ_{ex}. The chemical potential of ideal gas is trivial to calculate. To compute the excess part μ_{ex}, we further write it as an ensemble average,

$$\mu_{\mathrm{ex}} = -kT \ln\left(\frac{1}{V}\left\langle\int \exp\left(-\frac{\Delta U}{kT}\right)\mathrm{d}\mathbf{r}_{N+1}\right\rangle_N\right), \quad (6)$$

where ΔU is the potential energy change during insertion, $\Delta U(\mathbf{r}^N, \mathbf{r}_{N+1}) = U(\mathbf{r}^{N+1} = \{\mathbf{r}^N, \mathbf{r}_{N+1}\}) - U(\mathbf{r}^N)$. Notice the difference between $\mathbf{r}_i$ and $\mathbf{r}^N$. $\mathbf{r}_i$ denotes the position of the ith atom, while $\mathbf{r}^N$ contains the coordinates of all atoms in the configuration, which has a dimension of $3N$. The notation $\langle\cdots\rangle_N$ means the canonical ensemble average of a N-particle system

$$\langle A\rangle_N = \frac{\int A \exp[-U(\mathbf{r}^N)/kT]\mathrm{d}\mathbf{r}^N}{\int \exp[-U(\mathbf{r}^N)/kT]\mathrm{d}\mathbf{r}^N}. \quad (7)$$

In practice, the evaluation of Eq. (6) involves the calculation of two averages, namely the ensemble average $\langle\cdots\rangle_N$ and the spatial average $\int \exp(-\Delta U/kT)\mathrm{d}\mathbf{r}_{N+1}/V$. The ensemble average can be achieved by picking snapshots of configurations $\mathbf{r}^N$ randomly from MD or MC trajectories, while the spatial average is calculated by thoroughly scanning over $\mathbf{r}_{N+1}$, the position of the additional particle, in each snapshot.

B. Selective sampling

An obvious way to calculate the spatial average would be to carry out a uniform random sampling of the additional particle in the $\mathbf{r}_{N+1}$ space. However, this is not a very practical approach. In practice, one can sample only a limited number of positions, and few of them would actually fall in the low energy region of interest. In the end, such a random sampling could turn out to be extremely expensive and wasteful. Therefore an efficient sampling scheme is essential to avoid the random-sampling catastrophe.

It is more useful to regard the average in Eq. (6) as an one-dimensional integral over the insertion energy ΔU, i.e.,

$$\mu_{\mathrm{ex}} = -kT \ln\left(\int_{-\infty}^{+\infty} \rho(\Delta U)\exp\left(-\frac{\Delta U}{kT}\right)\mathrm{d}(\Delta U)\right), \quad (8)$$

where $\rho(\Delta U)$ is the probability density defined as

$$\frac{1}{V}\left\langle\int \delta(U(\{\mathbf{r}^N, \mathbf{r}_{N+1}\}) - U(\mathbf{r}^N) - \Delta U)\mathrm{d}\mathbf{r}_{N+1}\right\rangle_N. \quad (9)$$

Notice again that $\langle\cdots\rangle_N$ is the canonical ensemble average of a N-particle system, according to Eq. (7).

In order to determine accurately the right-hand side of Eq. (8), one has to produce good estimates of the values of $\rho(\Delta U)$ for the range of ΔU over which the product $\rho(\Delta U)\exp(-\Delta U/kT)$ takes on its large values. In other words, the sampling should be exclusively focused on the region near the cavities that can accommodate the additional particle at a small energy cost.

Here, we give an example of liquid copper at 2000 K (see Fig. 1). Since chemical potential is determined by the area below the curve $\rho(\Delta U)\exp(-\Delta U/kT)$, which decays exponentially in high-ΔU region, we introduce here an energy ceiling (e.g., $\Delta U = 0.6$ eV in the figure) to focus on the study of low-ΔU region, ignoring the rest. The energy ceiling is simply determined as a value where the product $\rho(\Delta U)\exp(-\Delta U/kT)$ becomes negligible, thus the converged excess chemical potential μ_{ex} is captured at the lowest computational cost, which is proportional to the area below the probability density curve. (Throughout the text, we choose as reference state (zero level in energy) the enthalpy of Cu(s) at 298 K and zero pressure,

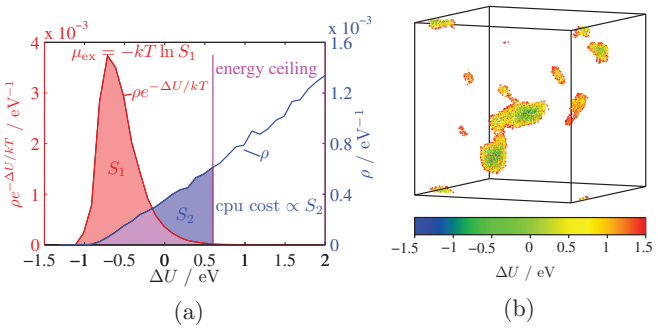

FIG. 1. (a) Probability density $\rho(\Delta U)$ and the product $\rho(\Delta U)\exp(-\Delta U/kT)$ of liquid copper at 2000 K. (b) Volumetric display of the insertion energy ΔU for a single snapshot in configuration $\mathbf{r}^N$. The colored region with low ΔU contributes most to the chemical potential, despite of its small size and correspondingly modest computational cost, compared to the whole cube.

which closely agrees with the definition employed in experiments.)

C. Algorithm

We propose here an algorithm to efficiently find the cavities and calculate the spatial average. For a N-particle configuration $\mathbf{r}_0^N$ in a parallelepiped, the integral can, in principle, be evaluated numerically on a uniform grid,

$$\frac{1}{V}\int \exp\left(-\frac{\Delta U\left(\mathbf{r}_0^N, \mathbf{r}_{N+1}\right)}{kT}\right) d\mathbf{r}_{N+1} = \frac{1}{N_a N_b N_c}\sum_{i,j,k=1}^{N_{a,b,c}} \exp\left(-\frac{\Delta U\left(\mathbf{r}_0^N, \mathbf{r}_{N+1}=\mathbf{r}_{ijk}\right)}{kT}\right), \quad (10)$$

where

$$\mathbf{r}_{ijk} = \frac{i}{N_a}\mathbf{a} + \frac{j}{N_b}\mathbf{b} + \frac{k}{N_c}\mathbf{c}. \quad (11)$$

$\mathbf{a}$, $\mathbf{b}$, $\mathbf{c}$ are the vectors defining the parallelepiped. Instead of running *ab initio* calculations on all grid points, we employ the following algorithm to search for cavities and to study the potential energy surfaces near them.

Let Fig. 2 be the potential energy (ΔU) surface near the cavity of interest. We find this cavity and map out the nearby potential energy surface in four steps.

1. Locate

We first estimate the position $\mathbf{r}_{N+1,0}$ of the cavity based on an approximate energy function. This function should tell us roughly where the cavity is, but does not need to be accurate, because it is never used to calculate the chemical potential. There are plenty of choices available to take this task. For example, an appropriate empirical potential is definitely sufficient to predict the position of the cavity. In practice, we find that even a function as simple as nearest neighbor distance can help locate the cavity, as shown in Fig. 3. This idea of prescreening has been successfully used before.[17,18]

2. Minimize

DFT calculation is performed at the predicted position $\mathbf{r}_{N+1,0}$. Based on the force calculated on the $(N+1)$th particle, the position is optimized as $\mathbf{r}_{N+1,1}$. This move attempt is checked by DFT, and will be accepted if $U(\{\mathbf{r}_0^N, \mathbf{r}_{N+1,1}\}) < U(\{\mathbf{r}_0^N, \mathbf{r}_{N+1,0}\})$. The optimization continues and generates a series of positions $\{\mathbf{r}_{N+1,i}, i = 1, 2, \ldots\}$, until the minimum is found. This procedure is equivalent to structure optimization under the constraint that all atoms are fixed

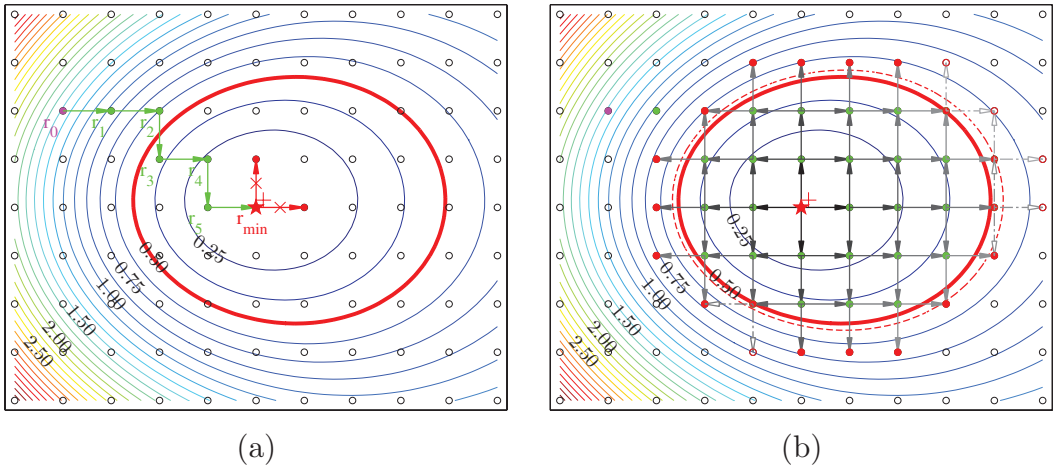

FIG. 2. Diagrammatic illustration of the algorithm in two dimensions. Assume the contour lines above represent the energy surface near the cavity we are interested in. (a) Step 1: We first estimate the position of the cavity (purple, $\mathbf{r}_{N+1,0}$) based on an approximate energy function. Step 2: Then DFT calculations are carried out and, based on the force calculated, the position of the $(N+1)$th particle (green, $\mathbf{r}_{N+1,i}$) is optimized, until the minimum grid point (red star, $\mathbf{r}_{N+1,\min}$) is found. The optimization proceeds as move attempts are accepted if $U(\{\mathbf{r}_0^N, \mathbf{r}_{N+1,i+1}\}) < U(\{\mathbf{r}_0^N, \mathbf{r}_{N+1,i}\})$. The green arrows are accepted move attempts, while the red ones are denied. (b) Step 3: All grid points below the energy ceiling (red circle) are studied with DFT, by gradually climbing up the energy surface from the bottom, until all frontier points (red solid dots) are above the energy ceiling. As a result, we need to calculate ΔU for the colored points only. Step 4: In case the dynamic energy ceiling needs to be increased (red dash circle), the "exploration" step restarts and demands additional calculations on new frontier points (red open dots).

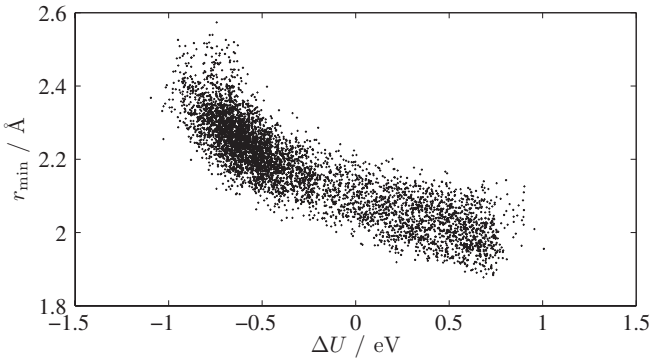

FIG. 3. Nearest neighbor distance analysis on 256 configurations $\mathbf{r}^N$ of liquid copper at 2000 K. The nearest neighbor distance $r_{\min}$ is calculated as the shortest distance from the grid point $\mathbf{r}_{ijk}$ to the N atoms and their periodic images. Large $r_{\min}$ corresponds to the center of a large cavity, which is optimal for particle insertion at a low energy cost.

except the last one, which is allowed to move only on grid points.

3. Explore

We explore the cavity by gradually climbing up the potential energy surface. If the bottom is lower than the energy ceiling, all its neighboring grid points will be studied. And if some of them are also below the ceiling, their neighbors will also be further calculated. This procedure spreads the "seeds" out, until all "seeds" hit the energy ceiling, which tells us that we have reached the inaccessible space region and there is no need to explore anymore. The exploration will end only if all points on the frontier of the cavity are above the energy ceiling.

4. Converge

An appropriate value for the energy ceiling is required in Step 3. However, unlike what has been discussed in Fig. 1, the probability density $\rho(\Delta U)$ is never known before we calculate it, rendering the energy ceiling *a priori* unknown. We circumvent this problem by introducing a dynamic, rather than static, energy ceiling. Starting from a relatively low trial value (e.g., −0.5 eV in Fig. 1), we first calculate the probability density below it (by Step 3), and then decide whether or not we should raise the energy ceiling, depending on the up-to-date $\rho(\Delta U)$ $\exp(-\Delta U/kT)$. The new energy ceiling, if it happens, may enclose some of the frontier points, thus restarting the exploration of the cavity (returning to Step 3). After the additional calculation is finished, the same question is asked again about whether to further increase the energy ceiling. Steps 3 and 4 are performed repeatedly, increasing the energy ceiling gradually and mapping out Fig. 1 from left to right, until the energy ceiling is high enough to give an excess chemical potential converged within some prespecified tolerance.

III. RESULTS

A. Chemical potential of liquid copper at 2000 K

We employ the scheme described above to calculate the chemical potential of liquid copper from first-principles. Before we describe the detailed methodology, we would like to first estimate the precision required in our calculation, because we want to further apply the results to the theoretical prediction of material properties, e.g., locating a melting point. We notice that the calculation of melting properties demands very high precision for chemical potentials. The melting temperature is determined by the intersection of chemical potential curves of a solid and a liquid. However, in practice these two curves usually cross at a shallow angle. Consequently, a small error in chemical potential may translate into a relatively large error in melting temperature. Typically, an error of 10 meV in chemical potential will result in an error of 100 K in melting point. Therefore, we need to make sure numerical and statistical errors are under control.

In the process of isochoric particle insertion, we use a periodic cube of edge length 11.66 Å with 108 copper atoms in it. All DFT calculations are performed using the Vienna *Ab-initio* Simulation Package (VASP),[19,20] with the projector-augmented-wave (PAW) implementation[21,22] and the generalized gradient approximation (GGA) for exchange-correlation energy, in the form known as Perdew-Burke-Ernzerhof (PBE).[23] Electronic temperature and its contribution to entropy are counted by imposing Fermi distribution of the electrons on the energy level density of states. The size of the plane-wave basis is carefully checked to reach the required accuracy. The energy cutoff (E_{cutoff}) is set to 273 eV in MD runs and particle insertion attempts. When we make corrections for pressure and energy, E_{cutoff} is increased to 500 eV, in order to remove Pulay stress (error in pressure within 1 kbar) and achieve convergence (error in energy within 1 meV) with respect to the basis size.

The sampling in k-space is also studied very carefully, to compromise between accuracy and computation cost. A dense k-point gird is necessary to meet the accuracy requirement. Indeed, we would like to use a 4 × 4 × 4 Monkhorst-Pack (MP) mesh in the first Brillouin zone (FBZ). However, since the point-group symmetry of our cubic supercell is broken by disorder, this would require all the 32 k-points included in the calculation, which is computationally too demanding. Kresse *et al.*[7] have addressed this problem by replacing the original 32 k-points with four special k-points in the irreducible FBZ, as if full cubic symmetry were still applied. This reduction can be well justified by the following argument. In the case of weak potential and nearly free electron gas, the dominant part in electronic Hamiltonian is the kinetic energy, which is approximately $\hbar^2/(2m_e)(\mathbf{G}+\mathbf{k})^2$ ($\mathbf{G}$ is a reciprocal lattice vector and $\mathbf{k}$ a k-point in FBZ), a term invariant under point-group operation with respect to the choice of $\mathbf{k}$. As simple metals are close to the free electron gas model, the same property should hold true, thus rationalizing the reduction of k-points by symmetry. Inspired by this idea and making a further improvement in which we seek a relatively even distribution of k-points in FBZ (while in the calculation of Kresse *et al.*, the k-space sampling focuses exclusively in the first octant), we represent the 4 × 4 × 4 MP grid by eight special k-points, whose coordinates are listed in Table I. To evaluate the accuracy, different k-space sampling methods are tested on ten randomly chosen MD

TABLE I. Comparison of different k-space sampling in terms of computational cost and error (in unit of meV/atom).

k-space sampling	Number	Error in MD	Error in ΔU
Γ point	1	46	106
MP $2 \times 2 \times 2$	4	2	6
MP $4 \times 4 \times 4$	32	<0.1	1
8 special k-points[a]	8	<0.1	3
4 special k-points[b]	4	0.5	19

[a]The coordinates of the k-points are: (1/8 1/8 1/8), (−3/8 1/8 1/8), (1/8 −3/8 1/8), (−1/8 −1/8 3/8), (−1/8 3/8 3/8), (3/8 −1/8 3/8), (−3/8 −3/8 1/8), (3/8 3/8 3/8).
[b]The coordinates and weights of the k-points are: (1/8 1/8 1/8), 1/8; (3/8 1/8 1/8), 3/8; (3/8 3/8 1/8), 3/8; (3/8 3/8 3/8), 1/8.

configurations (calculated as $U(\mathbf{r}^N)/N$) and insertion attempts (calculated as $\Delta U = U(\mathbf{r}^{N+1}) - U(\mathbf{r}^N)$). As Table I shows, sampling with the eight special k-points is comparable to the $4 \times 4 \times 4$ MP grid, while the computational cost is significantly reduced by a factor of four.

The ensemble average is computed numerically by running *ab initio* MD simulations within a canonical (*NVT*) ensemble with the Nosé-Hoover chain thermostat.[24–27] The MD simulation proceeds with a time step of 3 fs and lasts for 1280 steps. Forces acting on atoms are accurately calculated, as the convergency threshold for electronic structure optimization is set to 1×10^{-8} eV/atom. We capture snapshots every 5 ionic steps from the MD trajectory, thus generating 256 snapshots in total, from which the ensemble average is evaluated. The configuration $\mathbf{r}^N$ in each snapshot is then studied by making particle insertion attempts, to compute the spatial average over $\mathbf{r}_{N+1}$. The spatial average is calculated numerically on a uniform $40 \times 40 \times 40$ grid, according to Eq. (10). Only on selected grid points *ab initio* insertion energies ΔU are calculated, following the efficient scheme we proposed in Sec. II C. Finally, we compute the chemical potential by combining the ensemble and spatial averages.

As shown in Table II, we "measured" the chemical potential of liquid copper at 2000 K five times, based on five independent MD trajectories. The Helmholtz free energy change during particle insertion $\Delta F_{N\to N+1}$ is -1.273 ± 0.011 eV.

The selective calculation scheme helps us reduce the computational cost drastically. Instead of running *ab initio* calculations on all 1.6×10^7 grid points, the scheme demands calculations on only 5×10^3 grid points, reducing the computational cost by a factor of 3×10^3 and thus making the computation possible.

Now we make correction for the finite-size effect, which was alluded to earlier in Eqs. (1) and (3). Several analytical expressions have been proposed[28,29] for this type of correction. Despite of the differences, they all share the same leading term, $-(\partial p/\partial \rho)/(2N)$, where ρ is the density of particles. Here, we would like to account for the finite-size effect in the

TABLE II. Calculation of Helmholtz free energy change $\Delta F_{N\to N+1}$ by particle insertion. (Cu, 2000 K, $N = 108$, $a = 11.66$ Å, in eV.)

$\overline{\mu}_{\text{ex}}$	0.748 ± 0.011
μ_{id}	-2.021
$\Delta F_{N\to N+1}$	-1.273 ± 0.011

$$\boxed{N, T, p_1, V} \xrightarrow[\text{particle insertion}]{\text{isochoric}} \boxed{N+1, T, p_2, V}$$

$$\mu(V, T, N) = \Delta F_{N\to N+1} - (p_2 - p_1) \cdot V/(2N)$$

FIG. 4. Finite-size correction to the calculation of chemical potential by isochoric particle insertion method.

following way. The flaw of isochoric particle insertion lies in the fact that the next higher-order derivative may be significant and has to be included, which can be seen from the following Taylor expansion:

$$\begin{aligned}\Delta F_{N\to N+1} &= F(V, T, N+1) - F(V, T, N), \\ &\doteq \mu(V, T, N) + \frac{1}{2} \left.\frac{\partial \mu(V, T, n)}{\partial n}\right|_{n=N}, \end{aligned} \quad (12)$$

where $\Delta F_{N\to N+1}$ is the free energy change computed from particle insertion, $\mu(V, T, N)$ is the exact chemical potential, and $(\partial \mu/\partial n)$ is the leading correction term. Notice that this term is large for condensed phase materials, i.e., when n increases, μ will change significantly, as a result of the large increase in pressure. Simplifying the expression, we have the finite-size correction

$$\frac{\partial \mu(V, T, n)}{\partial n} = \frac{\partial \mu(p, T)}{\partial p} \cdot \frac{\partial p(V, T, n)}{\partial n} = \frac{V}{N}(p_2 - p_1), \quad (13)$$

$$\mu(V, T, N) = \Delta F_{N\to N+1} - \frac{V}{2N}(p_2 - p_1), \quad (14)$$

where p_1 and p_2 are the pressures before and after particle insertion, as shown in Fig. 4.

It is straightforward to show that this correction is equivalent to $-(\partial p/\partial \rho)/(2N)$, the leading term in the corrections proposed by Smit[28] and Siepmann[29]

$$-\frac{V}{2N}(p_2 - p_1) = -\frac{V}{2N}\frac{\partial p(V, T, n)}{\partial n} = -\frac{1}{2N}\frac{\partial p(V, T, n)}{\partial \rho}. \quad (15)$$

Another type of finite-size effect can be understood as the following. Compared to an infinite system, the test particle inserted in a small box will interact with its periodic images. In the case of charged atoms, the image charge interaction can be very large due to the long-range Coulomb interaction. In our small periodic model, image interactions must be examined to make sure that they are small enough to be neglected. To estimate this effect, we perform particle insertion tests on a 864-atom system (eight times larger than our original model) and make comparisons with the original results. The calculated insertion energies ΔU differ only by less than 3 meV. Thus, it is safe to neglect the weak image interactions in our model.

We have now calculated $\mu(p_1, 2000\ \text{K})$. We further convert $\mu(p_1, T)$ to $\mu(p^\circ = 1\ \text{bars} \simeq 0\ \text{kbar}, T)$, the chemical potential at standard atmospheric pressure, to simplify the comparison of our theoretical results with experiments

$$\mu_{p_1\to p^\circ} = \mu(p^\circ, T) - \mu(p_1, T) \simeq -\frac{p_1 V}{N}. \quad (16)$$

TABLE III. Theoretical chemical potential of liquid copper at 2000 K (in eV, $N = 108$, $a = 11.66$ Å, $p_1 = 5.5$ kbar, $p_2 = 10.6$ kbar).

$\Delta F_{N\to N+1}$	-1.273 ± 0.011
$-(p_2 - p_1)V/(2N)$	-0.023
$-p_1 V/N$	-0.050
$\mu(p^\circ, 2000\,\mathrm{K})$	-1.347 ± 0.011
$\mu(p^\circ, 2000\,\mathrm{K}, \mathrm{exp.})$	-1.342

The chemical potential is finally computed by combining Widom's particle insertion method and the corrections for finite-size effect and non-zero pressure

$$\mu(p^\circ, T) = \Delta F_{N\to N+1} - \frac{V}{2N}(p_2 - p_1) - \frac{p_1 V}{N}. \quad (17)$$

As shown in Table III, the theoretical chemical potential is predicted to be -1.347 ± 0.011 eV, which agrees very well with the experimental value -1.342 eV.

B. Chemical potential at various temperatures

The Gibbs free energies G at different temperatures and pressures are connected by the following thermodynamic relations:

$$\left[\frac{\partial(G/T)}{\partial(1/T)}\right]_p = H\,, \quad \left[\frac{\partial G}{\partial p}\right]_T = V. \quad (18)$$

Since enthalpy H and volume V can be obtained directly from MD simulation, free energy changes among different (p, T) conditions can be readily computed by thermodynamic integration method.

We start from the calculated $\mu(p^\circ, 2000\,\mathrm{K})$ and map out the chemical potential curve in region $T \in [1300, 2000]$ K and zero pressure. To compute enthalpy H in Eq. (18), *ab initio* canonical (NVT) MD simulation is performed at various temperatures in the region. Detailed settings in DFT calculations and MD thermostat have been described in Sec. III A. Enthalpy is calculated as an average of energies over MD trajectory at each temperature. Volume search is conducted to make sure $p \simeq 0$ kbar. As shown in Table IV, the calculated enthalpy and chemical potential agree very well with experiments.

TABLE IV. Enthalpies and chemical potentials of liquid copper (in eV/atom).

T	H	H_{exp}	μ	μ_{exp}
2000	...	...	-1.347 ± 0.011	-1.342
1950	0.642	0.645	-1.297 ± 0.011	-1.292
1850	0.609	0.611	-1.198 ± 0.010	-1.194
1750	0.575	0.577	-1.102 ± 0.010	-1.097
1650	0.540	0.543	-1.007 ± 0.009	-1.002
1550	0.505	0.509	-0.914 ± 0.009	-0.910
1450	0.470	0.475	-0.824 ± 0.008	-0.819
1350	0.434	0.441	-0.736 ± 0.008	-0.731

C. Calculation of melting temperature

The chemical potential of liquid copper is further used to calculate the theoretical melting temperature, which is determined by the intersection of chemical potential curves of the solid and of the liquid. The chemical potential of solid is computed within the quasiharmonic approximation[30] and is further corrected by thermodynamic integration (to account for anharmonicity at high temperatures). Phonon density of states, vibrational free energies, and thermal expansion are calculated using the "supercell" method as implemented in the Alloy Theoretic Automated Toolkit (ATAT).[31,32] Anharmonicity effect is included as further correction through the thermodynamic integration method, in which MD simulation is carried out with an effective Hamiltonian

$$H_\lambda = (1 - \lambda)H_\alpha + \lambda H_\beta \quad (19)$$

that gradually switches from the Hamiltonian H_α of a harmonic potential surface to the real Hamiltonian H_β. The chemical potential difference is calculated as

$$\mu^\beta = \mu^\alpha + \frac{1}{N}\int_0^1 \langle H_\beta - H_\alpha\rangle_\lambda \mathrm{d}\lambda, \quad (20)$$

where $\langle A\rangle_\lambda$ is the average of observable A in MD simulation with Hamiltonian H_λ.

The chemical potentials of solid and liquid copper, from both theory and experiment, are shown in Fig. 5. Compared with experiments, the errors of liquid and solid are -5 and -11 meV, respectively, in the melting region. The calculated melting temperature is 1440 K, about 80 K higher than the experimental value. This error is translated from both solid and liquid chemical potentials, as a combined effect. Since we focus mostly on the calculation of liquid chemical potentials in this article, we are more concerned about the impact purely from the liquid part, which is more accurate than the solid part and thus should lead to a smaller error. Indeed, the errors in melting point caused by solid and by liquid are 120 and -40 K, respectively, as shown in Fig. 5.

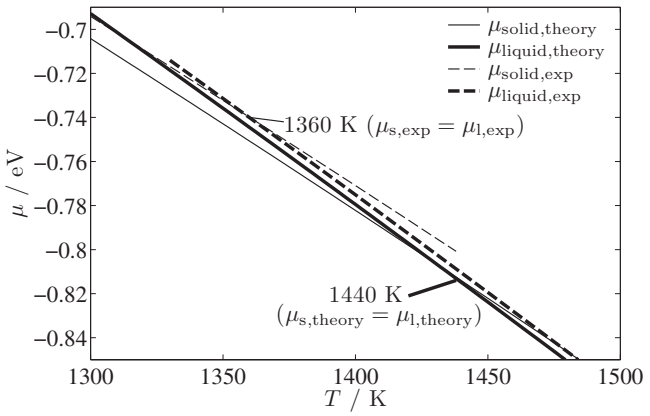

FIG. 5. Determine melting temperature from where solid and liquid chemical potential curves intersect on a μ-T plot. T_{m} from experiments is 1360 K. According to the liquid chemical potential we calculated by Widom's method, the theoretical T_{m} is 1320 or 1440 K, depending on whether we use experimental or theoretical results for the chemical potential of solid.

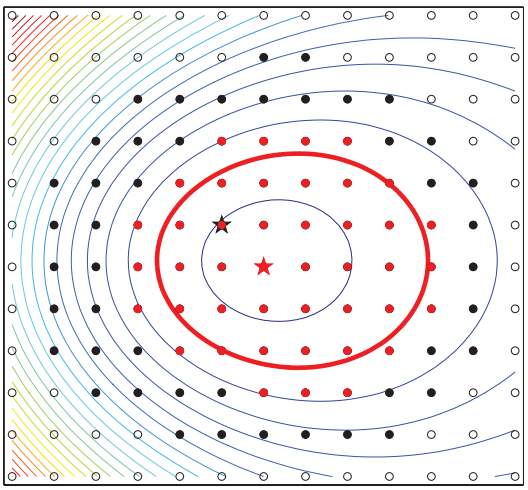

FIG. 6. This two-dimensional energy surface illustrates why our four-step algorithm works more efficiently than pre-screening. While traditional pre-screening labels all colored (both red and black) points as "important" based on the approximate energy model, the "locate" step in our algorithm outputs only the approximate minimum (a single grid point at the black star). Then the cavity is studied by the "minimize" and "explore" steps relying on *ab initio* calculations. As a result, our scheme calculates only the red points, and significantly cuts the unnecessary cost (all the surrounding black points).

IV. DISCUSSIONS AND CONCLUSIONS

Although the "locate" step in our algorithm appears to be similar to pre-screening, it is different in many aspects. Working in *ab initio* context, which is computationally much more expensive than empirical potentials, we need to design an algorithm highly selective about what should be calculated by DFT. In traditional pre-screening, the approximate energy model is used to find an approximate cavity that must completely enclose the true cavity, so the pre-screening criterion must necessarily be conservative and the more accurate/expensive energy model is invoked too often. The key distinction in our scheme is that the approximate energy model is only used to find a trial point at or near a cavity. The shape of the cavity is instead determined in the "explore" step relying on *ab initio* calculations and the only "wasted" calculations are those immediately at the boundary of the cavity. In traditional pre-screening, the set of "wasted" calculation points is three-dimensional, while in our scheme it is two-dimensional. An example is shown in Fig. 6. We save costs on several layers of black points, which are labeled as "important" by pre-screening but proven to be unnecessary by our algorithm.

One may argue that near the boundary of the cavity there could exist multiple minima, which could be ignored by mistake in our algorithm. Although it is true theoretical, this is very unlikely to happen in reality. First of all, if the multiple minima are connected by path lying below the energy ceiling, we will not miss them in the "explore" step. In the case of multiple minima not connected, we will miss them only if the "locate" step provides a single starting point when there should have been more than two. But this is not only very rare but also insignificant, because only small-size shallow cavities can escape from the examination of the "locate" step. Furthermore, the multiple minima issue is more a numerical convergence aspect than a fundamental limitation. As the ceiling is dynamically increased up to convergence, all minima that were previously missed will eventually be connected to existing cavities by a path below the energy ceiling.

Although the absolute error in DFT energies is likely larger than our target accuracy of 10 meV/atom, we benefit from the fact that our results (the melting point and chemical potentials relative to a reference state) are actually functions of energy differences between states of similar atomic densities and average coordination number, so that considerable error cancellation is to be expected.

Potential DFT errors aside, we are very careful about controlling the errors both from numerical and statistical origins. The errors in the *ab initio* calculations are mainly due to electronic structure calculations implementation details, e.g., the use of PAW method, the size of basis set, and k-space sampling. These problems have been carefully handled and discussed either in the above paragraph, or in Sec. III A. The errors in statistical methods are caused by detailed physical approaches to calculate the chemical potentials of the solid and of the liquid, i.e., quasi-harmonic approximation, thermodynamic integration, and Widom's particle insertion method. Because the chemical potentials of two phases are calculated with different statistical mechanics methods, we have to make sure that the calculations achieve absolute convergence with respect to the methods, since there is no chance that errors of the two phases will cancel.

Due to computational cost issues of DFT calculations, our chemical potential calculations can be performed only on a small system with around 100 atoms. The error caused by the small system size is studied systematically, as we gradually increase the system size and check the convergence. We first note that this error is inherent in the physical method of particle insertion itself and is irrelevant to the DFT formalism. Therefore, it is better to work with empirical potentials, as it is a practical way to test our method on large system size, without losing the accurate description of interatomic interactions. We implement the particle insertion method into the large-scale atomic/molecular massively parallel simulator package (LAMMPS)[33] to automate and accelerate the calculations. Two embedded atom model (EAM) potentials, namely copper (Mendelev, 2008)[34] and tantalum (Y.-H. Li, 2003),[35] are tested on system size up to 2000 atoms. The results are shown in Fig. 7. We find the chemical potential finally converges after we increase the system size beyond 1000 atoms. With the system size of approximately 100 atoms, the finite size error is 10−20 meV. Considering the huge computation cost we have to pay to work on larger systems from first principles, this amount of error is still acceptable.

The convergence with respect to grid resolution is studied with the same empirical potentials. We have tested different grid resolutions up to eight times denser than the grid in our reported DFT calculations. We analyze the results in two levels, namely the integral I (or spatial average mentioned before in Eq. (10)) in each individual snapshot and the chemical potential μ according to Eq. (6), which is related to the ensemble average of the above-mentioned integrals I, $\mu = -kT \ln \langle I \rangle_N$. Errors of spatial average in individual snapshots are

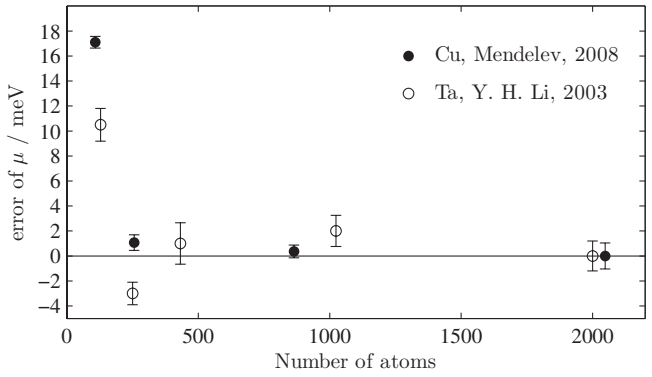

FIG. 7. Finite size error of chemical potential calculations, tested on two empirical potentials. The errors are 17 and 11 meV for Cu (108 atoms) and Ta (128 atoms), respectively.

plotted in Fig. 8 (blue cross). Although for a single snapshot it requires a very fine grid to achieve convergence, the error mostly cancels out in the ensemble average, therefore the chemical potential calculated from them converges quickly with respect to the grid resolution, as shown in Fig. 8 (red circle). We find that the results have already converged with a 40 × 40 × 40 grid, which is employed in our DFT calculations.

The success or failure of the particle insertion scheme depends heavily on whether sufficiently many large cavities are sampled and explored. Therefore, higher temperatures are preferable, since rare events occur more frequently (configurations with large cavities usually locate in the high-energy region of phase space and are rarely visited). We find that it is much easier to measure the chemical potential at 2000 K than at 1500 K. At the latter temperature, the chemical potential is significantly overestimated by a few tens of meV due to the lack of large cavities explored during the limited time of MD simulation.

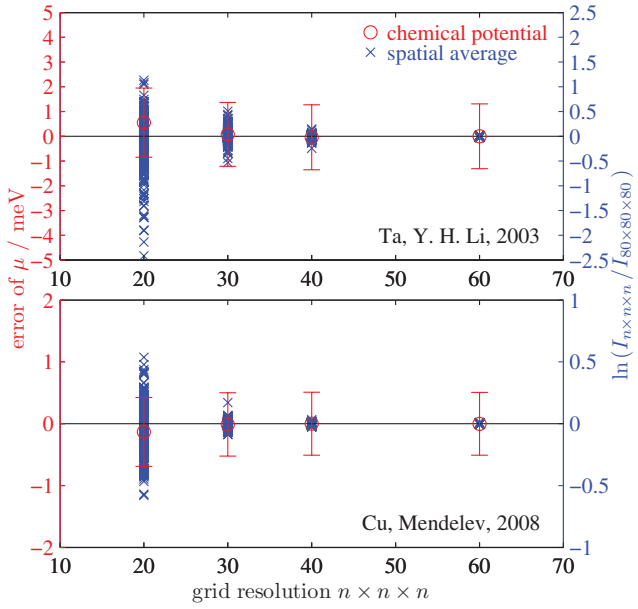

FIG. 8. Convergence tests carried out on different grids. Results from the densest grid (80 × 80 × 80) are chosen as benchmarks. The error of each single snapshot integral $I_{n\times n\times n}$ is calculated as $\ln(I_{n\times n\times n}/I_{80\times 80\times 80})$. Chemical potentials converge quickly with respect to grid resolution.

The method is easily generalizable to multi-component system, since one can compute the chemical potential of each species separately and exploit their partial molar property to obtain the Gibbs free energy of the phase from $\sum_i n_i\mu_i$. The only exception to this simple approach occurs when there are large electrostatic interactions that give rise to sharply varying free energies as a function of deviations from perfect stoichiometry, so that finite size effects are highly non-negligible. In this case, one way to avoid this issue is to insert multiple particles simultaneously to preserve stoichiometry, in which case the method would directly provide the Gibbs free energy of the phase, at the expense of higher computational requirements because the integrals become $3 \times \sum_{i=1}^{m} n_i$ dimensional (for $A_{n_1}B_{n_2}\cdots M_{n_m}$).

In this article, we demonstrate that it is computationally practical to calculate chemical potential of a liquid directly from first principles using a modification of Widom's particle insertion method. This, to the authors' knowledge, is the first attempt to evaluate the chemical potential of a liquid without the help of any high-quality empirical potentials, which are available only for a limited number and type of materials. This distinct advantage is crucial when such empirical potentials are difficult to obtain, e.g., for multi-component materials. An algorithm is proposed to efficiently find and study cavities. It reduces the computational cost drastically, e.g., by more than three orders of magnitude for the example we study, relative to Widom's original method. After finite-size correction, the calculated chemical potential of liquid copper at 2000 K is −1.347 eV, only 5 meV lower than the corresponding experimental value. This result is used to further map out the chemical potential curve of liquid-state copper as a function of temperature at zero pressure, by the thermodynamic integration method. Finally, a melting point is predicted by locating the intersection of the calculated chemical potential curves of the solid and of the liquid. The error in calculated melting temperature is 80 K.

ACKNOWLEDGMENTS

Discussions with Ligen Wang and Ljubomir Miljacic are gratefully acknowledged. This research was supported by the ONR (Grant Nos. N00014-12-1-0196 and N00014-10-1-0660) and by the NSF through TeraGrid and XSEDE resources provided by the NCSA, SDSC, and TACC.

[1]D. Frenkel and B. Smit, *Understanding Molecular Simulation* (Academic, San Diego, 1996).
[2]D. Kofke and P. Cummings, Mol. Phys. **92**, 973 (1997).
[3]P. Hohenberg and W. Kohn, Phys. Rev. B **136**, B864 (1964).
[4]W. Kohn and L. J. Sham, Phys. Rev. B **140**, 1133 (1965).
[5]R. Jones and O. Gunnarsson, Rev. Mod. Phys. **61**, 689 (1989).
[6]O. Sugino and R. Car, Phys. Rev. Lett. **74**, 1823 (1995).
[7]G. de Wijs, G. Kresse, and M. Gillan, Phys. Rev. B **57**, 8223 (1998).
[8]D. Alfè, M. Gillan, and G. Price, Nature (London) **401**, 462 (1999).
[9]D. Alfè, G. Price, and M. Gillan, Phys. Rev. B **65**, 165118 (2002).
[10]D. Alfè, G. De Wijs, G. Kresse, and M. Gillan, Int. J. Quantum Chem. **77**, 871 (2000).
[11]B. Widom, J. Chem. Phys. **39**, 2808 (1963).
[12]S. Romano and K. Singer, Mol. Phys. **37**, 1765 (1979).

[13]K. S. Shing and K. E. Gubbins, Mol. Phys. **46**, 1109 (1982).
[14]D. Moller and J. Fischer, Mol. Phys. **69**, 463 (1990).
[15]A. Lotfi, J. Vrabec, and J. Fischer, Mol. Phys. **76**, 1319 (1992).
[16]J. Anwar, D. Frenkel, and M. Noro, J. Chem. Phys. **118**, 728 (2003).
[17]J. Forsman and B. Jonsson, J. Chem. Phys. **101**, 5116 (1994).
[18]J. Kim, R. L. Martin, O. Rubel, M. Haranczyk, and B. Smit, J. Chem. Theory Comput. **8**, 1684 (2012).
[19]G. Kresse and J. Furthmüller, Comput. Mater. Sci. **6**, 15 (1996).
[20]G. Kresse and J. Furthmüller, Phys. Rev. B **54**, 11169 (1996).
[21]P. Blöchl, Phys. Rev. B **50**, 17953 (1994).
[22]G. Kresse and D. Joubert, Phys. Rev. B **59**, 1758 (1999).
[23]J. Perdew, K. Burke, and M. Ernzerhof, Phys. Rev. Lett. **77**, 3865 (1996).
[24]S. Nosé, Mol. Phys. **52**, 255 (1984).
[25]S. Nosé, J. Chem. Phys. **81**, 511 (1984).
[26]W. G. Hoover, Phys. Rev. A **31**, 1695 (1985).
[27]G. J. Martyna, M. L. Klein, and M. Tuckerman, J. Chem. Phys. **97**, 2635 (1992).
[28]B. Smit and D. Frenkel, J. Phys. Condens. Matter **1**, 8659 (1989).
[29]J. Siepmann, I. McDonald, and D. Frenkel, J. Phys. Condens. Matter **4**, 679 (1992).
[30]A. van de Walle and G. Ceder, Rev. Mod. Phys. **74**, 11 (2002).
[31]A. van de Walle, M. Asta, and G. Ceder, CALPHAD: Comput. Coupling Phase Diagrams Thermochem. **26**, 539 (2002).
[32]A. van de Walle, CALPHAD: Comput. Coupling Phase Diagrams Thermochem. **33**, 266 (2009).
[33]S. J. Plimpton, J. Comp. Phys. **117**, 1 (1995).
[34]M. I. Mendelev, M. J. Kramer, C. A. Becker, and M. Asta, Philos. Mag. **88**, 1723 (2008).
[35]Y. H. Li, D. J. Siegel, J. B. Adams, and X. Y. Liu, Phys. Rev. B **67**, 125101 (2003).